SCIENTIFIC REP🔴RTS

Substrate specificity of human MCPIP1 endoribonuclease

Mateusz Wilamowski[1], Andrzej Gorecki 🆔[2], Marta Dziedzicka-Wasylewska[2] & Jolanta Jura[1]

MCPIP1, also known as Regnase-1, is a ribonuclease crucial for regulation of stability of transcripts related to inflammatory processes. Here, we report that MCPIP1 acts as an endonuclease by degrading several stem-loop RNA structures and single-stranded RNAs. Our studies revealed cleavage sites present in the stem-loops derived from the 3′ untranslated region of the interleukin-6 transcript. Furthermore, MCPIP1 induced endonuclease cleavage at the loop motif of stem-loop structures. Additionally, we observed that MCPIP1 could cleave single-stranded RNA fragments. However, RNA substrates shorter than 6 nucleotides were not further affected by MCPIP1 nucleolytic activity. In this study, we also determined the dissociation constants of full-length MCPIP1$_{D141N}$ and its ribonuclease domain PIN D141N with twelve oligonucleotides substrates. The equilibrium binding constants (Kd) for MCPIP1$_{D141N}$ and the RNA targets were approximately 10 nM. Interestingly, we observed that the presence of a zinc finger in the PIN domain increases the affinity of this protein fragment to 25-nucleotide-long stem-loop RNA but not to shorter ones. Furthermore, size exclusion chromatography of the MCPIP1 and PIN proteins suggested that MCPIP1 undergoes homooligomerization during interaction with RNA substrates. Our results provide insight into the mechanism of MCPIP1 substrate recognition and its affinity towards various oligonucleotides.

Ribonuclease degradation of mRNA is an essential mechanism to control the level of selected transcripts in cells. MCPIP1 (Monocyte Chemoattractant Protein-1–Induced Protein 1), also known as Regnase1, regulates RNA stability through its ribonucleolytic activity. Regulation of immune responses by MCPIP1 occurs through the direct degradation of transcripts of many cytokines, such as IL-1β, IL-2, IL-6, IL-8, IL-12b, and IL-17[1–7]. MCPIP1 was described as a modulator of inflammatory processes in the early phase of inflammation[5]. MCPIP1 also regulates differentiation, tumor growth and angiogenesis[8–10].

The enzymatic activity of MCPIP1 is due to the PIN domain (PilT N–terminus), which possesses ribonucleolytic activity[1,2]. The putative MCPIP1 active site consist of four aspartate residues that are engaged in coordination of a single magnesium ion localized in the enzyme catalytic cleft[11]. PIN domains are commonly present in various eukaryotic and prokaryotic nucleases that cleave different classes of RNA molecules, including mRNA, rRNA, tRNA and viral RNAs[12,13]. One of those nucleases is the Dis3 subunit of the eukaryotic exosome complex, which contains a PIN domain that has endonuclease activity against mRNA. Additionally, the C-terminal domain of Dis3 possesses processive 3′ to 5′ exonuclease activity[14]. PIN domains are frequently present as the toxin agent of prokaryotic proteins engaged in toxin-anti-toxin systems, including the VapBC system containing the VapC PIN ribonuclease[15]. Recently, the *Caenorhabditis elegans* protein REGE-1 was shown to contain a functional nuclease PIN domain, indicating close homology to MCPIP1[16].

MCPIP1, which is encoded by *ZC3H12A*, belongs to the MCPIP family comprising products of the genes *ZC3H12A*, *ZC3H12B*, *ZC3H12C* and *ZC3H12D*[17]. A specific feature shared by this family is a single CCCH zinc finger (ZF) domain positioned at the C-terminal region of the PIN ribonuclease domain. CCCH-type ZFs are characteristic of proteins involved in RNA processing. Several representatives of CCCH ZF RNA-binding proteins are tristetraproline (TTP), Roquin1 and Roquin2[18]. The CCCH ZF increases the efficiency of RNA substrate cleavage catalyzed by MCPIP1[11,19]. Additionally, the crystal structure of the PIN domain revealed the positively charged loop sequence that is located near the catalytic core of MCPIP1. This loop may mediate the interaction with negatively charged phosphate groups of oligonucleotide backbones[11]. Homooligomerization of MCPIP1 occurs through the C-terminal domain, which is enriched in proline residues. Deletion of this region decreased ribonucleolytic activity of MCPIP1[20]. Purified recombinant MCPIP1 protein with a mutation in the nuclease

[1]Department of General Biochemistry, Faculty of Biochemistry, Biophysics and Biotechnology, Jagiellonian University, Krakow, Poland. [2]Department of Physical Biochemistry, Faculty of Biochemistry, Biophysics and Biotechnology, Jagiellonian University, Krakow, Poland. Correspondence and requests for materials should be addressed to J.J. (email: jolanta.jura@uj.edu.pl)

Name	Sequence	Length
RNA oligonucleotides		
mIL-6$_{82-106}$ 3′FAM	5′-UGUUGUUCU<u>CUACGA</u>AGAACUGACA-3′-FAM	25 nt
mIL-6$_{82-106}$ 5′FAM	FAM-5′-UGUUGUUCU<u>CUACGA</u>AGAACUGACA-3′	25 nt
mIL-6$_{82-106}$ RS	FAM-5′-**ACAGUCAAGA**<u>CUACGA</u>**UCUUGUUGU**−3′	25 nt
mIL-6$_{82-106}$ YR	FAM-5′-UGUUGU**ACA**<u>CUACGA</u>**UGU**ACUGACA-3′	25 nt
mIL-6$_{85-101}$ short stem	FAM-5′-UGUUCU<u>CUACGA</u>AGAAC-3′	17 nt
hIL-6$_{82-99}$	FAM-5′-UGUUCUC<u>UAUGG</u>AGAACU-3′	18 nt
consensus stem-loop	FAM-5′-UGGAAAG<u>UAU</u>CUUUCCU-3′	17 nt
mIL-6$_{82-93}$	FAM-5′-UGUUGUUCUCUA-3'	12 nt
mIL-6$_{82-88}$	FAM-5′-UGUUGUU-3'	7 nt
poly-U	FAM-5′-UUUUUUUUUUUU-3'	12 nt
mIL-6$_{82-106}$ int. ACA	FAM-5′-UGU**ACA**UCU<u>CUACGA</u>AGA**UGU**UACA-3′	25 nt
mIL-6$_{83-98}$ ter. ACA	FAM-5′-**ACA**GUUCUC<u>UAUGG</u>AGAAC**UGU**−3′	22 nt
mIL-6$_{85-93}$ ter. ACA	FAM-5′-**ACA**UGUUCUCUA-3′	12 nt
mIL-6$_{1-45}$	FAM-5′-UGCGUUAUGCCUAAGCAUAUCAGUUU GUGGACAUUCCUCACUGUG-3′	45 nt
DNA oligonucleotides		
mIL-6$_{82-93}$ ssDNA	FAM-5′-TGTTGTTCTCTA-3′	12 nt
mIL-6$_{82-93}$ dsDNA	FAM-5′-TGTTGTTCTCTA-3′ 3′-ACAACAAGAGAT-5′	12 bp

Table 1. Nt sequences of fluorescently modified oligonucleotides used for the RNase assays and affinity determination assays. Nts that form loop fragments of stem-loop structures are underlined. Sequences with numbered residues are part of the 3′UTR of transcripts from mouse or human IL-6. These sequences were numbered such that the first nt after the stop codon of the coding sequence is marked as 0. RS – reverse stem modification of mIL-6$_{82-106}$ (altered nts are in bold). YR – purine and pyrimidine residue modification of mIL-6$_{82-106}$ (altered nts are in bold).

catalytic site (D141N) retained the ability to recognize RNA, and formation of the nucleoprotein complex was observed in gel shift electromobility assays[19,21].

The half-life of transcripts is primarily modulated through RNA-binding proteins that recognize *cis*-regulatory elements, such as AU-rich elements (AREs) or stem-loop structures. MCPIP1 recognizes stem-loops in mRNA and degrades transcripts in an ARE-independent manner[1,2,4]. Analyses of sequences obtained from high-throughput sequencing of RNA isolated by crosslinking immunoprecipitation (HITS-CLIP) showed that stem-loop sequences preferably recognized by MCPIP1$_{D141N}$ contain pyrimidine-purine-pyrimidine (YRY) loop motifs[5]. These results indicated that the MCPIP1 ribonuclease recognizes sequences present in certain structural motifs. Interestingly, MCPIP1 and Roquin cooperate in posttranscriptional gene regulation by processing the same set of target mRNAs[5,22]. The YRY sequence motif was also previously identified in targets recognized by Roquin1, which binds stem-loop RNA[23]. However, Roquin1 itself does not possess nuclease activity, and regulation of transcripts occurs through the recruitment of the CCR4-NOT deadenylase complex[24].

Many transcripts that were determined in high-throughput sequencing analysis as a transcript negatively regulated by MCPIP1 do not possess the YRY motif in the loop structure of stem-loops. Moreover, some of these transcripts were also validated as targets for MCPIP1-induced degradation. It was shown that fragments derived from 3′UTR of the transcripts coding for interleukin-2 121–140, BCL2L1 and BIRC3 deprived of YRY motif in the stem loops are not targets for MCPIP1 induced degradation.[4,9] Interestingly, MCPIP1 has potential to recognize the stem-loop sequences with a wide range of sizes. For example, the reported consensus sequence from HITS-CLIP analysis is 7 nt-3 nt-7 nt (stem-loop-stem)[5]. However, validated as a target for MCPIP1 the stem loop from 3′UTR transcript coding for mouse STAT3 1739–1765 contains 10 nt-8 nt-10 nt (stem-loop-stem) motif [25]. Therefore, it is possible that MCPIP1 recognizes loop sequences with various nucleotide (nt) content and structures. Thus, in this study, we focused on describing the specificity of MCPIP1 substrate recognition using RNA cleavage assays and affinity determination assays.

Results

Determination of substrate specificity for MCPIP1.   We purified recombinant human MCPIP1$_{WT}$ and MCPIP1$_{D141N}$, which were expressed in *E. coli* cells. The purity of the analyzed proteins was confirmed by SDS-PAGE analysis (Supplementary Fig. S1). To define the MCPIP1 nuclease substrate specificity, we performed RNase cleavage assays using 4 types of oligonucleotides: 17-25-nt-long RNA forming stem-loop structures (mIL-6$_{82-106}$, mIL-6$_{85-101}$ short stem, hIL-6$_{82-99}$), 7-12-nt-long single-stranded RNA (mIL-6$_{82-93}$, mIL-6$_{82-88}$), 12-nt-long single-stranded DNA (mIL-6$_{82-93}$ ssDNA) and 12-nt-long double-stranded DNA (mIL-6$_{82-93}$ dsDNA). These sequences were derived from the 3′ untranslated region (UTR) of the IL-6 transcript. Furthermore, we also analyzed consensus stem-loop sequences that were previously identified as MCPIP1 targets[5] and single-stranded poly-U RNA sequences. Detailed information about the applied oligonucleotide sequences is presented in Table 1.

Because the activity of MCPIP1 is dependent on the presence of Mg^{2+} or Mn^{2+} metal ions, all degradation assays were performed in buffer with the divalent cation Mg^{2+}. Additionally, to decrease non-specific electrostatic
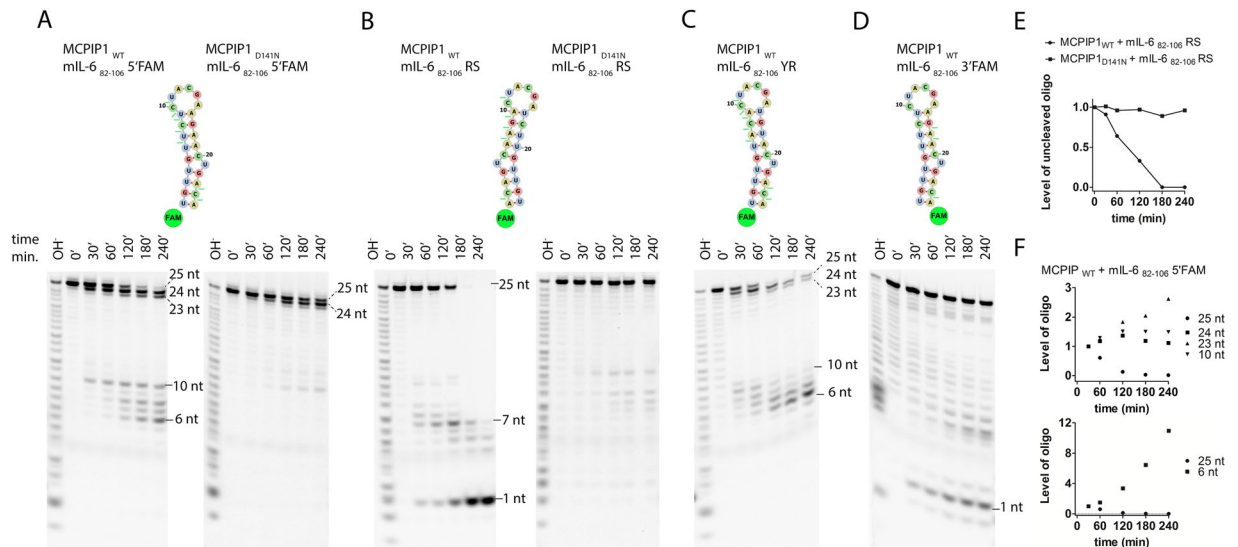
Figure 1. RNA fragments obtained upon MCPIP1-catalyzed cleavage. (**A**) Sequences and structures of the 25-nt-long RNA stem-loops derived from the mIL-6$_{82-106}$ 3′UTR fragment are depicted. (**B**) Degradation assay of the modified mIL-6$_{82-106}$ stem-loop (RS – reverse stem alteration). (**C**) Degradation assay of the modified mIL-6$_{82-106}$ stem-loop (YR – pyrimidine and purine alterations). (**D**) Degradation assay of the mIL-6$_{82-106}$ stem-loop labeled at the 3′ end. The oligonucleotides were labeled at the 5′ or 3′ end with FAM dye. The reaction products were resolved on 20% denaturing PAGE and visualized with a fluorescence imaging system. Concentrations of the labeled oligonucleotides and MCPIP1 protein were 7.5 μM and 2 μM, respectively. The D141N mutation of a conserved aspartate of the PIN domain catalytic center of the MCPIP1 decreased its ribonucleolytic activity. (**A–D**) Were made by the separation of gels that are shown at Supplementary Fig. S2A,D. Major sites of MCPIP1-induced cleavage are indicated by the oligonucleotide fragment length. (**E**) Densitometric analysis of the kinetics of RNA degradation presented as the level of the remaining uncleaved oligonucleotides from the RNase assay. The graph shows the level of the stem-loop sequence: mIL-6$_{82-106}$ RS during degradation. (**F**) Densitometric analysis of the MCPIP1$_{WT}$ induced degradation of the mIL-6$_{82-106}$ 5′FAM oligonucleotide. Analysis was carried out separately for each of degradation products of the mIL-6$_{82-106}$ 5′FAM. Oligonucleotide levels were normalized at the time 30 min.

interactions between MCPIP1 and nucleic acids, the cleavage studies were performed at physiological salt concentration (150 mM NaCl). The observed MCPIP1 ribonuclease activity products were reproducibly consistent for proteins obtained from different batches.

In each case, the RNA cleavage assay was carried out for 30, 60, 120, 180 and 240 minutes. We initially performed an RNase assay of the mIL-6$_{82-106}$ stem-loop structure. We observed that MCPIP1$_{WT}$ induced degradation starting from the 3′ end of the mIL-6$_{82-106}$ 5′FAM, and MCPIP1$_{WT}$ cleaved the 25th single nt as the first one. Then, the 24th nt was cleaved (Fig. 1A). Simultaneously, mIL-6$_{82-106}$ 5′FAM stem-loop cleavage occurred at the loop site, between the C10 and U11 nts (Fig. 1A). In the consequence, a 10 nt single-stranded RNA fragment was generated from the 5′ end of the mIL-6$_{82-106}$ 5′FAM stem-loop structure. Next, additional processive degradation of the nascent 10-nt-long ssRNA was observed (Fig. 1A). However, MCPIP1-induced degradation was not observed for ssRNA fragments consisting of 6 nt (Fig. 1A).

Next, to verify the stereospecificity of MCPIP1-induced cleavage, we reversed the sequence of the mIL-6$_{82-106}$ at the stem site of this stem-loop. Surprisingly, after reversing the stem sequences (mIL-6$_{82-106}$ RS oligonucleotide), we observed a single nt product induced by MCPIP1$_{WT}$ activity, indicating that enzymatic hydrolysis occurred between first (A) nt and the second (C) nt (Fig. 1B). Thus, the reverse stem sequence (mIL-6$_{82-106}$ RS) was cleaved between the same nts as the basic mIL-6$_{82-106}$ stem-loop, in which MCPIP1$_{WT}$ triggered enzymatic hydrolysis between A$_{25}$ and C$_{24}$ nt in the vicinity of the 3′ end of the oligonucleotide (Fig. 1A,B). Moreover, accumulation of the 7-nt-long degradation product of the mIL-6$_{82-106}$ RS oligonucleotide indicated that MCPIP1$_{WT}$ introduced cleavage between the A$_7$ and A$_8$ nts (Fig. 1B).

We also examined whether the analysis of oligonucleotide degradation was affected by potential *E. coli* contaminants remaining from the protein purification procedure. Therefore, we analyzed oligonucleotide cleavage induced by MCPIP1$_{D141N}$ with a substitution of the conserved aspartate at the catalytic center of the PIN domain. No ribonucleases activity of the MCPIP1$_{D141N}$ was observed for the mIL-6$_{82-106}$ RS stem-loop oligonucleotide (Fig. 1B,E). However, low-efficacy nuclease activity of MCPIP1$_{D141N}$ was observed for mIL-6$_{82-106}$ 5′FAM, as shown in Fig. 1A. MCPIP1$_{D141N}$ induced cleavage occurred only at 3′ end of this oligonucleotide. Thus, the D141N mutation does not completely abolish *in vitro* enzymatic activity of MCPIP1.

The characteristic feature of the unmodified mIL-6$_{82-106}$ stem-loop is a high presence of pyrimidine residues at the 5′ site of the stem. Therefore, to assess the role of this characteristic pattern, we modified the stem sequence to achieve balanced distribution of the purine and pyrimidine residues at the stem site of this stem-loop. Nts 6–9 and 16–19 were changed in mIL-6$_{82-106}$ YR (Table 1 and Fig. 1C). Our results showed that MCPIP1$_{WT}$-induced
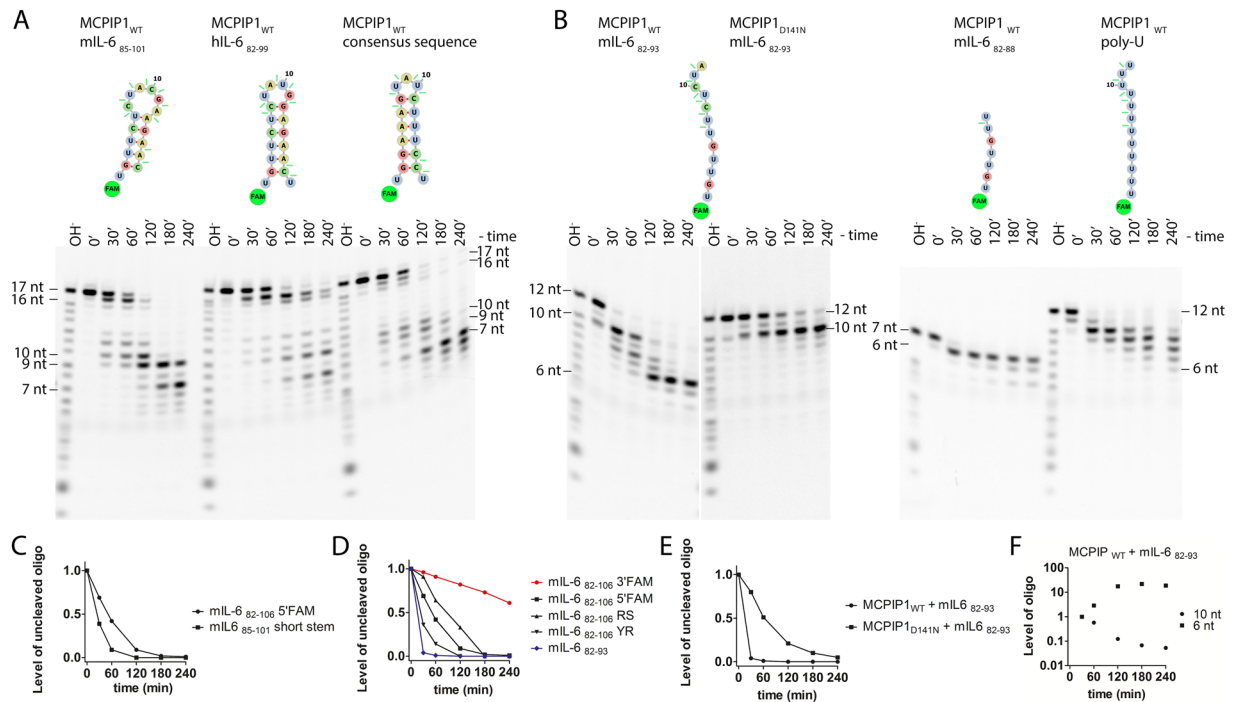
Figure 2. RNA fragments obtained upon cleavage catalyzed by MCPIP1. Major sites of MCPIP1-induced cleavage are indicated by the oligonucleotide fragment length. (**A**) Sequences and structures of the short stem-loops are depicted. These sequences form 17-18-nt-long stem-loops. (**B**) Degradation of the single-stranded RNAs. Twelve and 7-nt-long single-stranded RNA sequences were part of the mIL-6_{82-106} stem-loop. Poly-U homopolymer RNA contains 12 uracil residues. The oligonucleotides were labeled at the 5′ end with FAM dye. The reaction products were resolved on 20% denaturing PAGE and visualized with a fluorescence imaging system. Concentrations of the labeled oligonucleotides and MCPIP1 protein were 7.5 μM and 2 μM, respectively. The D141N mutation of a conserved aspartate of the PIN domain catalytic center of the MCPIP1 decreased its ribonucleolytic activity. (**A,B**) Were made by the separation of gels that are shown at Supplementary Fig. S2B–D. (**C**) Densitometric analysis of the level of the remaining uncleaved oligonucleotides from the RNase assay at different time points. The panel shows a comparison of the kinetics of degradation of the mIL-6_{82-106} and a shorter fragment of this stem-loop, which is mIL-6_{85-101}. (**D**) The panel shows the level of degradation of the 25-nt-long stem-loop mIL-6_{82-106} in comparison with the 12 nt ssRNA sequence of the mIL-6_{82-93}. (**E**) The graph compares the degradation of the ssRNA mIL6_{82-93} with MCPIP1$_{WT}$ or MCPIP1$_{D141N}$, which possesses attenuated RNase activity. (**F**) Densitometric analysis of the MCPIP1$_{WT}$ induced degradation of the mIL-6_{82-93} oligonucleotide. The analysis was carried out for 6 nt and 10 nt long mIL-6_{82-93} degradation products respectively, oligonucleotide levels were normalized at the time 30 min.

degradation of the mIL-6_{82-106} YR occurs at the same time at the loop site of the stem-loop structure or at the 3′ end of the stem-loop structure (Fig. 1C). Furthermore, we determined that after destabilization of the mIL-6_{82-106} YR stem loop structure through loop cleavage induced by MCPIP1$_{WT}$, the 10-nt-long ssRNA was increased and subsequently processively degraded (Fig. 1C). Additionally, we observed that degradation of mIL-6_{82-106} YR stops at the fragment consisting 6 nt, similar to the degradation of the unmodified mIL-6_{82-106} 5′FAM oligonucleotide (Fig. 1A,C). Alteration of purine with pyrimidines (mIL-6_{82-106} YR) did not change the cleavage sites in the stem loop structure, and degradation was triggered as in the case of mIL-6_{82-106} 5′FAM (Fig. 1A,C). Thus, we concluded that MCPIP1$_{WT}$-induced *in vitro* degradation is not dependent on stem sequence of the stem-loop.

To avoid negative results due to diminished cleavage susceptibility of sites where nts are modified by fluorescent labeling, we labeled the mIL-6_{82-106} stem-loop structure at the 5′ end or 3′ end (mIL-6_{82-106} 5′FAM, mIL-6_{82-106} 3′FAM, respectively). For the mIL-6_{82-106} 3′FAM sequence, we observed a 1-nt-long degradation product; therefore, the first cleavage induced by MCPIP1$_{WT}$ occurs between C_{24} and A_{25} nts as shown in Fig. 1D. Thus, cleavage between C_{24} and A_{25} was observed for both the mIL-6_{82-106} 5′FAM and mIL-6_{82-106} 3′FAM sequences. However, for the 3′FAM-labeled oligonucleotide, the degradation was less efficient. Comparison of Fig. 1A,D suggests that the presence of fluorescent dye on a cleaved nt does not significantly affect the MCPIP1 activity.

Kinetics of oligonucleotide degradation triggered by MCPIP1 depends on many factors. In the next step, we examined whether the stem-loop structure, oligonucleotide length or nucleotide sequence affected MCPIP1 nucleolytic efficiency. To verify the impact of different stem-loop structures and sequences on MCPIP1-triggered cleavage, we used a set of short stem-loops consisting of 17 or 18 nts (mIL-6_{85-101}, hIL-6_{82-99}, consensus stem-loop) (Table 1). We observed that MCPIP1$_{WT}$ induced cleavage of two nts from the 3′ end of these oligonucleotides and also accumulation of bands that are 10, 9 and 7 nt long (Fig. 2A). These findings indicated

that MCPIP1$_{WT}$ introduces endonucleolytic cleavage in the loop region of those short stem-loops (mIL-6$_{85-101}$, hIL-6$_{82-99}$, consensus stem-loop). Initial MCPIP1$_{WT}$-induced enzymatic hydrolysis occurs simultaneously for four phosphodiester bonds between 9–12 nt at the loop motif of the mIL-6$_{85-101}$ sequence (Fig. 2A). We determined that the pattern of loop cleavage of the mIL-6$_{85-101}$ stem-loop is different than that for mIL-6$_{82-106}$ 5′FAM, which was cut between the C10 and U11 nts (Fig. 1A). Therefore, the stem length of the stem-loop affects the cleavage sites recognized by MCPIP1.

To verify the influence of size of high-order RNA backbone structures on the oligonucleotide cleavage rates, we performed kinetic analysis. The kinetics of oligonucleotide degradation are shown as the level of uncleaved oligonucleotides obtained from densitometric analysis of the results from oligonucleotide degradation assays. In the subsequent time points of the RNase assay, uncleaved mIL-6$_{85-101}$ oligonucleotide levels were significantly decreased compared to uncleaved levels of the mIL-6$_{82-106}$ oligonucleotides (Fig. 2C). We observed that MCPIP1$_{WT}$-triggered cleavage of the mIL-6$_{85-101}$ stem-loop was relatively faster than that of the hIL-6$_{82-99}$ stem-loop, which possesses longer stems (Fig. 2A). These results showed that the kinetics of degradation of RNA stem-loop structures containing short stems is faster than that of stem-loops possessing longer stems. We concluded that unwinding of shorter stems from the stem-loop structures results in a more efficient degradation (Figs 1A and 2A,C). To determine the importance of loop fragments in MCPIP1-triggered stem-loop cleavage, we compared stem-loops that contain a 3, 4 or 6 nt long loop motif. However, we did not observe major differences in MCPIP1-induced degradation of these oligonucleotides (Fig. 2A).

Subsequently, we assessed whether MCPIP1$_{WT}$ degrades unstructured ssRNA. After MCPIP1$_{WT}$-triggered destabilization of stem-loop structures, a subsequent cleavage occurred in the nascent ssRNA. Thus, we examined 12-nt-long ssRNA oligonucleotides from the mIL-6$_{82-93}$ and 7-nt-long mIL-6$_{82-88}$ ssRNA (Fig. 2B). Using the RNA folding software mFOLD[26], we confirmed that the mIL-6$_{82-93}$ and mIL-6$_{82-88}$ sequences did not show base pairing interactions at room temperature; thus, they do not fold into stable secondary structures. We noticed that for the unstructured ssRNA, the rate of MCPIP1$_{WT}$-induced degradation was increased compared to cleavage of the stem-loop sequences (Fig. 2D). Degradation of either mIL-6$_{82-93}$ or mIL-6$_{82-88}$ indicated that ssRNAs shorter than 6 ribonucleotides were not efficiently cleaved by MCPIP1$_{WT}$ (Fig. 2B). The levels of shortened oligonucleotides formed as a result of the MCPIP1$_{WT}$ induced cleavage of the mIL-6$_{82-106}$ 5′FAM indicated high increase of the 6 nt long truncated oligonucleotide (Fig. 1F). Furthermore, we observed 11-fold increase of the level of 6 nt product of the MCPIP1$_{WT}$ induced cleavage of the mIL-6$_{82-93}$ (Fig. 2F). Moreover, there was marginal catalytic activity of MCPIP1$_{D141N}$ for ssRNA, which presented as cleavage of two nts from the 3′ end of the mIL-6$_{82-93}$ oligonucleotide (Fig. 2B,E). To verify the sequence specificity of ssRNA cleavage, we performed degradation assays using poly-U sequences. However, it appeared that MCPIP1$_{WT}$ processively cleaved the poly-U homopolymer, and the oligonucleotide degradation stopped when the fragment consisted of 6 nt (Fig. 2B). These results indicated that MCPIP1$_{WT}$ cleaves unstructured ssRNA in a sequence-independent manner.

We next investigated whether MCPIP1 exhibits RNA substrate specificity. Therefore, in RNase cleavage assays, we used single-stranded and double-stranded DNA (ssDNA and dsDNA) as a substrate. These DNA sequences were similar to RNA sequences consisting of 12 nts present in the mIL-6$_{82-93}$ oligonucleotide. We observed that MCPIP1$_{WT}$ cleaves both ssDNA and dsDNA (Fig. 3A). Degradation of these sequences occurred from the 3′ end; however, the kinetics of these processes was lower compared with the cleavage of mIL-6$_{82-93}$ ssRNA (Figs 2B,E and 3A,B). Degradation of the mIL-6$_{82-93}$ ssDNA had approximately equal efficiency using either MCPIP1$_{WT}$ or MCPIP1$_{D141N}$ (Fig. 3A,B). Therefore, the aspartate 141 residue of MCPIP1 is crucial for RNA cleavage but not for DNA processing (Figs 1A,B, 2B and 3A,B).

We showed that MCPIP1$_{D141N}$ does not possess activity against mIL-6$_{82-106}$ RS (Fig. 1B). However, we have observed that MCPIP1$_{D141N}$ possesses low nuclease activity in some of the investigated systems (Figs 1A, 2B and 3A). Therefore, to further confirmation that presented RNA cleavage assay is not affected by contaminations from *E. coli* extract we used another control which is MCPIP1$_{438-599}$ protein deprived of PIN nuclease domain. Applying MCPIP1$_{438-599}$ to RNase assay we did not observe degradation of investigated oligonucleotides (Supplementary Fig. S2E). Thus, our results are not affected by contaminations and we conclude that single mutation D141N of MCPIP1 is not sufficient to completely abolish *in vitro* MCPIP1 nuclease activity. All identified cleavage sites observed in degradation assays are listed in Supplementary Table S1. To verify the sequence specificity of MCPIP1-triggered degradation of RNA, we presented the identified sites of cleavage as a consensus logo (Supplementary Fig. S3). For logotype preparation, we used the sequence logo generator software WebLogo[27]. We figured out that cleavage sites lacking G nts in the immediate vicinity of the cut site were preferable for MCPIP1-induced cleavage (Supplementary Fig. S3).

Observed at Fig. 1 oligonucleotides cleavage patterns and results presented at Supplementary Fig. S3 revealed possible MCPIP1 sequence specificity within 5′-ACA-3′ motif. To confirm this observation we prepared three additional oligonucleotides that contain 5′-ACA-3′ modifications (Table 1). The internal modification of stem sequence to 5′-ACA-3′ was introduced to the mIL-6$_{82-106}$ (Supplementary Fig. S2F). We observed that MCPIP1$_{WT}$ induced cleavage of the mIL-6$_{82-106}$ int. ACA occurs at loop site between the C10 and U11 nts, then, additional cleavages were spotted between A4-C5-A6 nts (Supplementary Fig. S2F). However, incorporation of terminal 5′-ACA-3′ to the hIL-6$_{83-98}$ sequence revealed that for this oligonucleotide MCPIP1$_{WT}$ induced cleavage takes place between sequences U5-U6-C7 (Supplementary Fig. S2F). For single stranded RNA addition of terminal 5′-ACA-3′ to the mIL6$_{85-93}$ showed that MCPIP1$_{WT}$ induces hydrolysis of bond between C2 and A3 nts of the mIL6$_{85-93}$ ter. ACA (Supplementary Fig. S2F). Nevertheless, processive 3′ to 5′ cleavage of single stranded RNA is highly efficient compared to endonuclease cleavage (Supplementary Fig. S2F).

To further confirmation of our observation about *in vitro* nonspecific cleavage of RNA oligonucleotides by MCPIP1$_{WT}$ we performed additional experiments. We checked whether MCPIP1$_{WT}$ might cleave the template which were previously reported at *in vivo* studies as not degraded by MCPIP1 nuclease activity. The fragment comprising 1–81 nt from the mIL-6 3′UTR is not regulated through MCPIP1 activity in cells studies[5]. The distal
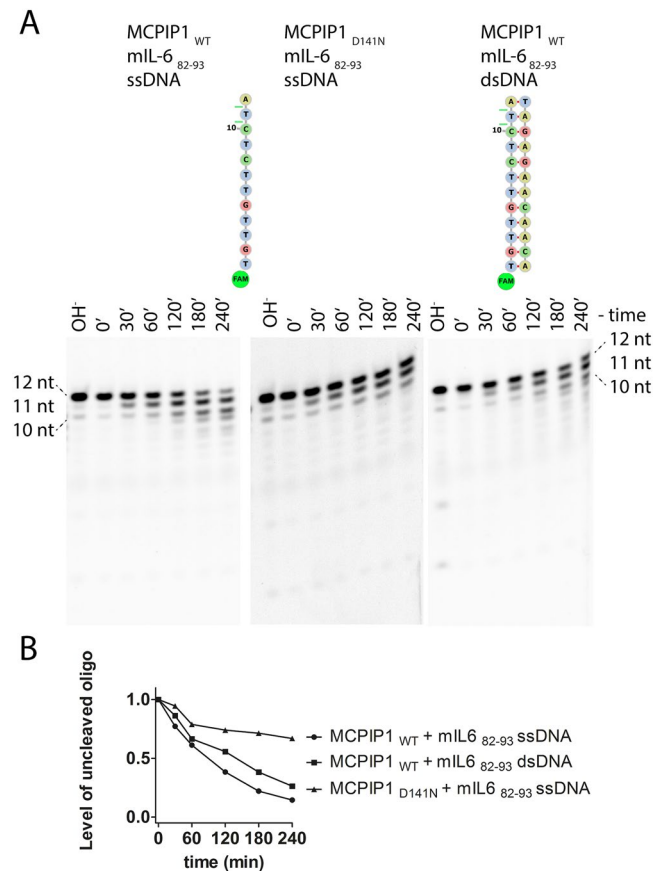
Figure 3. DNA fragments obtained upon cleavage catalyzed by MCPIP1. (**A**) The DNA sequences are based on the mIL-6$_{82-106}$ sequence; one oligonucleotide is ssDNA, and the second is dsDNA. The oligonucleotides were labeled at the 5′ end with FAM dye. The reaction products were resolved on 20% denaturing PAGE and visualized with a fluorescence imaging system. Concentrations of the labeled oligonucleotides and MCPIP1 protein were 7.5 μM and 2 μM, respectively. The D141N mutation of a conserved aspartate of the PIN domain catalytic center of the MCPIP1 decreased its ribonucleolytic activity. (**A**) Was made by the separation of gels that are shown at Supplementary Fig. S2C,D. (**B**) Densitometric analysis of the level of the remaining uncleaved ssDNA and dsDNA oligonucleotides from the MCPIP1 nuclease activity assay at different time points.

part of the mIL-6 3′UTR contains the mIL-6$_{82-106}$ 3′UTR stem loop which is the putative element responsible for IL-6 transcripts destabilization through MCPIP1 nuclease activity. Due to limitations of synthesis methodology we used 45 nts long sequence from the mIL-6$_{1-45}$ 3′UTR (Table 1 and Supplementary Fig. S2F). Using RNA folding software mFOLD[26] we showed that the mIL-6$_{1-45}$ oligonucleotide possibly forms two stem-loops structures as shown at Supplementary Fig. S2F. Degradation of the mIL-6$_{1-45}$ 3′UTR clearly indicates endonuclease activity of MCPIP1$_{WT}$. The fragment of the mIL-6$_{1-45}$ tends to form two stem-loop secondary structures, thus observed cleavage induced by MCPIP1$_{WT}$ should be introduced at loop site of these stem loops. Indeed we observed endonuclease cleavage of the mIL-6$_{1-45}$ at both loop sites (Supplementary Fig. S2F). However, due to obtained low electrophoresis resolution we could not precisely describe the exact nucleotides between which cleavage takes place (Supplementary Fig. S2F).

Dissociation constants of the MCPIP1 complex with oligonucleotides. Our results from oligonucleotide degradation assays did not reveal a strong structural or sequence preference of *in vitro* RNA cleavage by recombinant MCPIP1$_{WT}$. However, we determined that single-stranded RNA or 17-nt-long stem-loops were cleaved with a faster rate than 25-nt-long stem loops. For that reason, we investigated whether there were any differences in MCPIP1$_{D141N}$ affinity for the tested oligonucleotides. We used FAM-labeled oligonucleotides to develop a method for determination of the MCPIP1$_{D141N}$ affinity to oligonucleotides. Previously, we used electrophoretic mobility shift assays (EMSAs) to show that MCPIP1$_{D141N}$ has the potential to form stable complexes with 3′UTR fragments of the C/EBPβ transcript and obtained complexes possessing two distinct quaternary structures[21]. Observed shifts at EMSA assay indicated that the marginal nuclease activity of MCPIP1$_{D141N}$ did not repress formation of the nucleoprotein complex. Estimated binding affinities of the complexes of MCPIP1$_{D141N}$ with RNA based on our results published previously by Lipert *et al*. were between 640–1580 nM (Supplementary Table S2)[21]. The obtained Kd varies from previously used the 3′UTR sequence fragments of the C/EBPβ transcript. However, in our previous EMSA experiments, we were not able to determine the equilibrium dissociation constants of the achieved complexes.
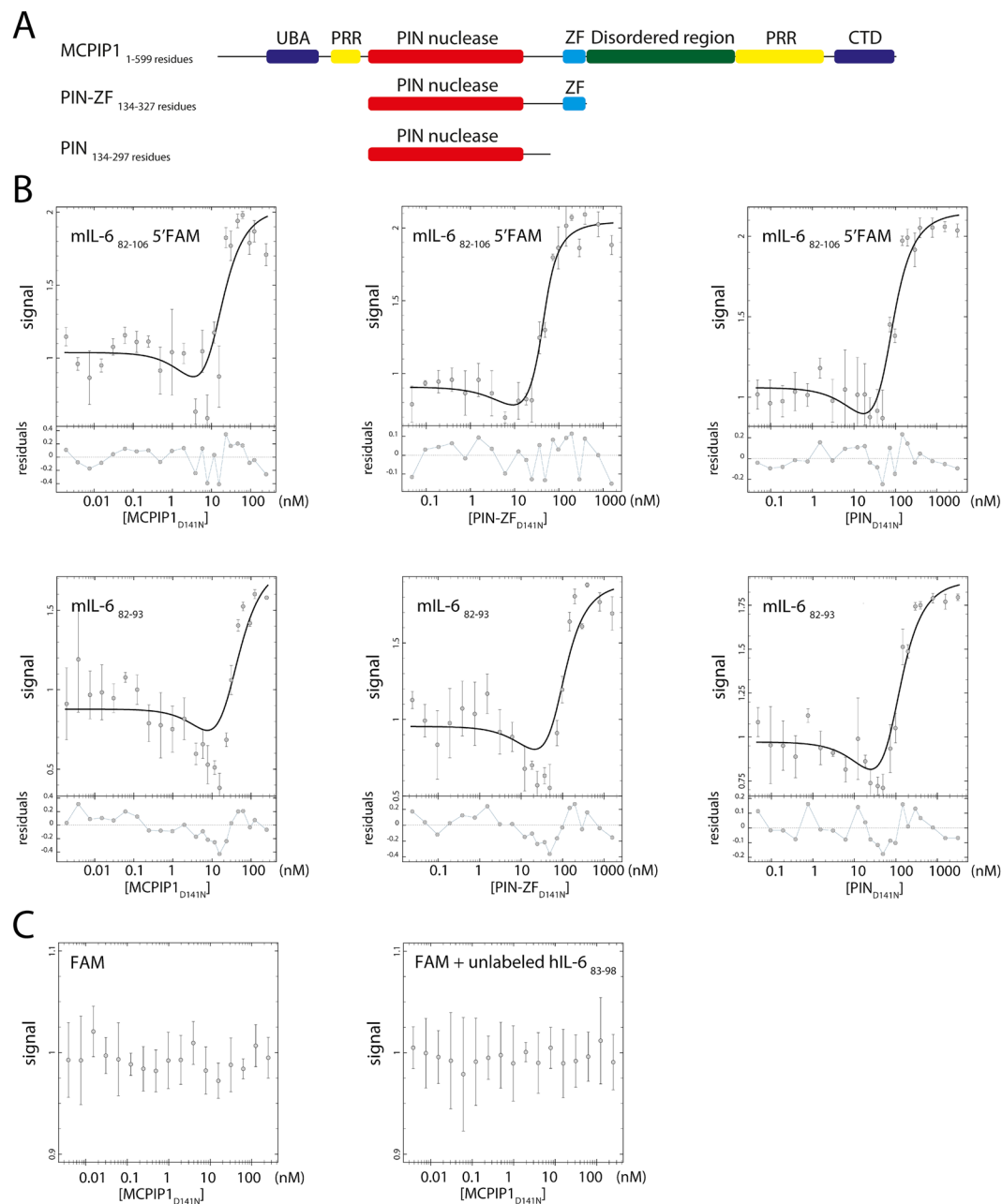
Figure 4. (**A**) Domain characterization of MCPIP1: UBA$_{43-89}$ (Ubiquitin-associated domain); PRR$_{100-126}$ and $_{458-536}$ (Proline-rich region); PIN$_{133-270}$ (PilT N-terminus nuclease domain); ZF$_{305-325}$ (zinc-finger motif); disordered region$_{326-457}$; CTD$_{545-598}$ (C-terminal conserved domain). Depicted fragments of MCPIP1, PIN-ZF and PIN that were used in presented studies. (**B**) Affinity of the MCPIP1 interaction with oligonucleotides forming RNA stem-loop structures: mIL-6$_{82-106}$ 5'FAM and single-stranded RNA oligonucleotides represented by mIL-6$_{82-93}$. The analyzed proteins were the catalytic mutated forms: MCPIP1$_{D141N}$ and its PIN-ZF$_{D141N}$ and PIN$_{D141N}$ fragments. The ribonuclease PIN$_{D141N}$ domain was studied without or with the zinc finger motif at the C-terminal region. Graphs illustrate the interaction of selected proteins (MCPIP1$_{D141N}$, PIN-ZF$_{D141N}$, and PIN$_{D141N}$) with oligonucleotides. Functions were fitted to the fluorescence intensity data points using the sequential binding model $N + P + P \rightleftarrows NP + P \rightleftarrows NPP$ (P – protein N – oligonucleotide). The depicted errors bars are standard deviations, n = 3. (**C**) Controls of the affinity determination assay. MCPIP1$_{D141N}$ in a presence of the free FAM label and unlabeled hIL-6$_{81-98}$ RNA oligonucleotide.

Herein, we determined the apparent equilibrium dissociation constants of the human MCPIP1$_{D141N}$ complexes with different types of oligonucleotides: stem-loop RNA, ssRNA, ssDNA and dsDNA (Fig. 4B, Supplementary Fig. S4 and Table 2). The slopes of dose-response curves were very steep for protein concentration values between 10 nM and 100 nM. Amplitudes of the fluorescence signals were changed approximately 2 times depending on the sequence. Fluorescence polarization assay which is commonly used for affinity determination might be affected by high fluorescence intensity changes observed in our measurements. Thus, we decided to

	MCPIP1$_{D141N}$ 1–599 aa K$_d$ (nM)	PIN-ZF$_{D141N}$ 134–327 aa K$_d$ (nM)	PIN$_{D141N}$ 134–297 aa K$_d$ (nM)
Stem-loop RNAs			
mIL-6$_{82–106}$ 5′FAM	6.5 ± 2.1[a]	6.6 ± 3.1[b]	24.1 ± 7.3[ab]
mIL-6$_{82–106}$ 3′FAM	8.6 ± 2.6[a]	4.8 ± 1.8[b]	21.8 ± 6.3[ab]
mIL-6$_{82–106}$ RS	9.8 ± 2.3[a]	15.1 ± 7.3[b]	39.3 ± 8.6[ab]
mIL-6$_{82–106}$ YR	9.5 ± 5.2[a]	14.4 ± 9.6	25.1 ± 7.0[a]
mIL-6$_{85–101}$ short stem	9.2 ± 4.0[a]	20 ± 10	20.7 ± 7.2[a]
hIL-6$_{82–99}$	4.1 ± 3.6[a]	13.2 ± 6.8	15.1 ± 4.5[a]
consensus stem-loop	3.8 ± 2.8[a]	9.1 ± 3.2[b]	36 ± 17[ab]
ssRNA			
mIL-6$_{82–93}$	19 ± 11[a]	34 ± 18	41 ± 12[a]
mIL-6$_{82–88}$	14.5 ± 8.1[a]	32 ± 20	40 ± 12[a]
poly-U	14.8 ± 7.2[a]	43 ± 23	39 ± 11[a]
mIL-6$_{82–93}$ ssDNA	18.3 ± 8.2	36 ± 20	21.7 ± 6.6
mIL-6$_{82–93}$ dsDNA	118 ± 49	80 ± 30	56 ± 17

Table 2. Calculated equilibrium dissociation constants of MCPIP1 complexes with selected oligonucleotides. The analyzed proteins were mutated forms of MCPIP1 and its ribonuclease domain (MCPIP1$_{D141N}$, PIN-ZF$_{D141N}$, and PIN$_{D141N}$). K$_d$ values were determined using DynaFit4 software with the implemented model of sequential binding of two proteins to a single oligonucleotide with a single dissociation constant. Errors are shown as standard deviations, n = 3. Statistical significance (P value < 0.05) between selected groups is shown by the following indexes: [a] and [b] for comparison of the MCPIP1$_{D141N}$ with PIN$_{D141N}$ and PIN-ZF$_{D141N}$ with PIN$_{D141N}$ groups, respectively. Differences observed between the MCPIP1$_{D141N}$ and PIN-ZF$_{D141N}$ groups are not statistically significant.

analyze only fluorescence intensity signal which also gives us better residuals of obtained fits. The two-phase course of fluorescence intensity changes, observed in all investigated cases, prompted us to model the affinity data with a complex double equilibrium binding equation where N + P + P ⇌ NP + P ⇌ NPP (N – oligonucleotide, P – protein) (Fig. 4B and Supplementary Fig. S4). These results showed that two protein molecules sequentially bind to a single oligonucleotide. The best model describing our data was a sequential binding model with equal equilibrium-binding dissociation constants, K$_{d1}$ = K$_{d2}$. We also analyzed the model characterized by K$_{d1}$ ≠ K$_{d2}$, which was rejected because it inconsiderably improved the residual distribution, however, the standard deviations of the calculated Kd were higher than those for the model with Kd$_1$ = Kd$_2$. A third analyzed model with a single equilibrium constant, N + P + P ⇌ NPP, was rejected because it had the highest residuals of curves that were fitted to the measured data points. The final selected model (sequential binding analysis, K$_{d1}$ = K$_{d2}$) reflects the measured data well, and the obtained K$_d$ are shown in Table 2. This model was characterized by the lowest standard deviation of the obtained dissociation constant values and low residuals of the fitted curves.

We observed that for the set of investigated oligonucleotides comprising stem-loop structures, ssRNA, and ssDNA, we did not find major differences between dissociation constants of the complexes with MCPIP1$_{D141N}$ (Table 2). Therefore, MCPIP1$_{D141N}$ can efficiently bind diverse oligonucleotide sequences. Minor differences in the MCPIP1$_{D141N}$ affinity to stem-loop structures or single-stranded oligonucleotides suggest that the nucleic acid double-stranded helical structure is not necessary to interact with MCPIP1. Additionally, we observed that MCPIP1 has lower affinity to dsDNA comparing to other investigated nts (Table 2). We showed that the affinity of full-length MCPIP1$_{D141N}$ to oligonucleotides is significantly higher than that for fragments of this protein represented only by the nuclease domain (PIN$_{D141N}$) (Fig. 4A,B, Supplementary Fig. S4 and Table 2). Moreover, we noticed that the zinc finger domain increased the affinity of the PIN$_{D141N}$ subunit to 25-nt-long oligonucleotides but not to shorter oligonucleotides (Fig. 4A,B, Supplementary Fig. S4 and Table 2).

Binding assays using free FAM dye did not showed significant changes of fluorescence intensity at investigated systems (Fig. 4C). MCPIP1$_{D141N}$ and buffer condition did not affect fluorescence emission of the free FAM label. The unlabeled hIL-6$_{81–98}$ RNA oligonucleotide did not affect fluorescence emission of free FAM label in the presence of MCPIP1$_{D141N}$ (Fig. 4C).Thus, we assume that described interactions are the effect of the assembly of the MCPIP$_{D141N}$ complex with oligonucleotides. The shape of fluorescence spectra of the FAM labeled oligonucleotides were consistent for all examined MCPIP1$_{D141N}$ concentrations (Supplementary Fig. S4A). Fluorescence intensity of the FAM labeled oligonucleotides were changed due to MCPIP1$_{D141N}$ nucleoprotein complex formation which affected FAM fluorescence probe (Supplementary Fig. S4A).

Observed dissociation constants for MCPIP1$_{D141N}$ complexes with mIL-6$_{82–106}$ 5′FAM were substantially weaker for EMSA system than in fluorescence based assay (Table 2, Supplementary Fig. S5 and Supplementary Table S2). We suppose that differences in dissociations constants are the results of the complex binding kinetics of MCPIP1 interaction with RNA that possibly is characterized by relatively fast k$_{off}$ rates. In case of high k$_{off}$ the EMSA as a non-equilibrium method will give higher dissociation constants compared to equilibrium techniques. The EMSA shift for mIL-6$_{82–93}$ ssRNA and mIL-6$_{82–93}$ ssDNA were observable at a relatively low concentration of MCPIP$_{D141N}$ (400 nM) (Supplementary Fig. S5A) although, at higher concentration of the MCPIP1$_{D141N}$ the oligonucleotides were not completely bounded in nucleoprotein complex. Therefore, we didn't calculate the Kd
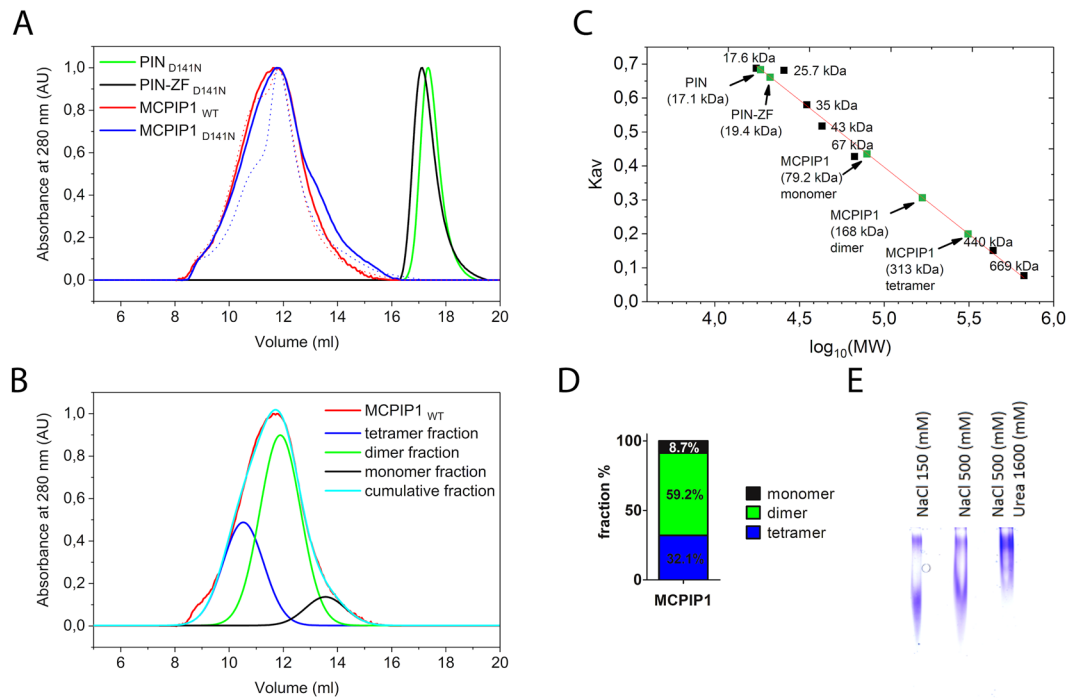
Figure 5. Homooligomerization of the MCPIP1 protein. (**A**) Size exclusion chromatography results of MCPIP1. Chromatography was performed in a buffer comprised of 25 mM Tris, pH 7.9, 300 mM NaCl, 10% (w/v) glycerol, 1 mM DTT, and 0.5 mM EDTA. Additionally, for results shown as a dotted line, the buffer was enriched in 1.6 M urea. (**B**) A multiple Gaussian peak fit was performed to model the obtained elution profile of MCPIP1$_{WT}$. Fitted peaks illustrated tetrameric, dimeric and monomeric fractions of the MCPIP1$_{WT}$. (**C**) Calibration curve of the gel filtration column. Green points indicate the apparent molecular weight of the investigated proteins calculated using the calibration curve. The molecular weights of these proteins are as follows: MCPIP1: 65.7 kDa; PIN-ZF: 24.7 kDa; PIN: 21.1 kDa. (**D**) Percentages of the MCPIP1$_{WT}$ tetrameric, dimeric, and monomeric fractions were calculated based on the area of the size exclusion chromatography peaks. (**E**) Native PAGE results of MCPIP1$_{WT}$ sample in buffers containing 50 mM Tris-HCl, pH 8.3, 150 mM NaCl, 10% (w/v) glycerol, 2.5 mM MgCl$_2$, 1 mM DTT, 0.5 mM EDTA and 0.05 mM ZnCl$_2$. Additional buffer condition changes were an increased concentration of NaCl to 500 mM and addition of urea to 1600 mM.

from that results. EMSA results might suggest that there are differences in quaternary structures of the complex between MCPIP1 D141N and different types of substrates (Supplementary Fig. S5A).

Homooligomerization of MCPIP1. Interestingly, the two-phase course of fluorescence intensity changes was observed in the obtained affinity assay graphs during oligonucleotide-binding processes (Fig. 4B, Supplementary Fig. S4). Thus, two protein molecules sequentially bind to a single RNA molecule. According to other studies, PIN domain superfamily proteins are frequently described as oligomers: dimers or tetramers[28]. Therefore, to obtain precise data of the MCPIP1 protein oligomerization state, we analyzed protein size exclusion chromatography results. In both cases, single Gaussian peaks were observed, indicating the monodispersity of the analyzed protein fragments. Analysis of protein size based on the retention volume (Fig. 5A,C) indicates that both the PIN and PIN-ZF domains were in a monomeric state. The mouse PIN domain was previously suggested to be a dimer[19]. In contrast, for full-length MCPIP1$_{WT}$ and MCPIP1$_{D141N}$, we observed wide elution peaks that shifted in favor of possible oligomeric forms (Fig. 5A). To assess these elution profiles, we performed multiple Gaussian peak fit analyses (Fig. 5B). Comparing the obtained maxima of fitted peaks with the column calibration curve, we observed that the calculated molecular masses of the fractions corresponded to tetrameric, dimeric and monomeric forms of MCPIP1$_{WT}$ (Fig. 5C,D). Therefore, the full-length MCPIP1$_{WT}$ or MCPIP1$_{D141N}$ is most frequently present as a dimer in native conditions, however, tetrameric and monomeric fractions were also present in solution (Fig. 5A–D). Buffer supplementation with 1.6 M urea resulted in narrowing peaks in size exclusion chromatography, indicating the additional increase of the MCPIP1 dimers fraction in the sample (Fig. 5A–D). Native PAGE electrophoresis of MCPIP1 revealed two heterogeneous bands for MCPIP1$_{WT}$ (Fig. 5E). These results confirmed that MCPIP1 homooligomerization occurs in native conditions. Equilibrium between the dimeric and tetrameric states of MCPIP1 could be influenced by changing the buffer composition. After addition of urea to the native PAGE buffer, the equilibrium was shifted in favor of the MCPIP1 tetrameric fraction (Fig. 5D). Urea as a chaotropic agent alternates hydrogen bonding between water molecules and proteins, and therefore affect hydrophobic interactions[29]. The small concentration of urea or other commonly used denaturation agent: guanidine hydrochloride increases stability of some proteins and might increase reactions rates[30]. Urea concentration (1.6 M) used in our experiment has a much lower concentration than typically is used
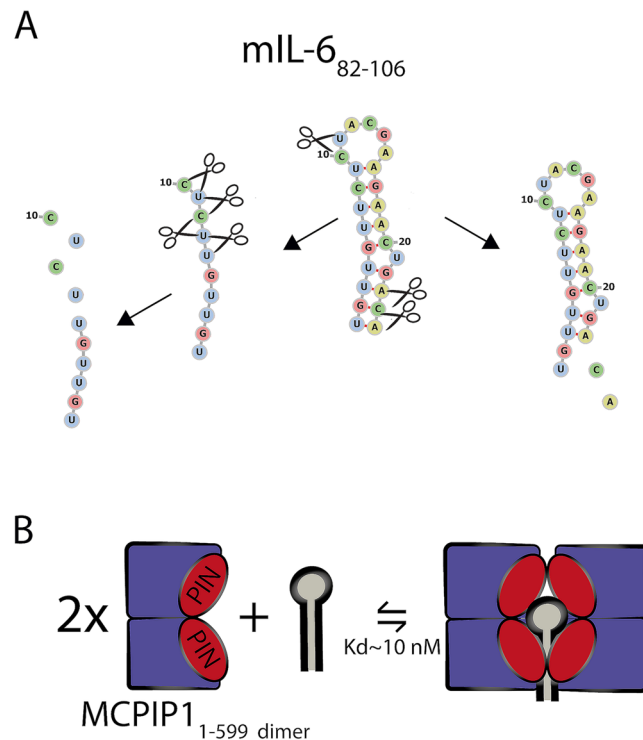
Figure 6. (**A**) Identification of MCPIP1-triggered cleavage sites in the mIL-6$_{82-106}$ stem-loop RNA structure. Nt sequences and structures created during MCPIP1-induced cleavage are illustrated. Mapping of the cleavage sites based on the RNase assay results, intermediates and the most significant subsequent degradation products are presented. (**B**) Visualization of the stoichiometry of the MCPIP1 interaction with stem-loops. Schematic cartoon representation of the ternary complex model. The size exclusion chromatography results showed that PIN and PIN-ZF were monomeric and suggest that full-length MCPIP1 most frequently occurs as a dimer in native condition. Stoichiometry of the MCPIP1 - RNA interaction was based on the size exclusion chromatography results and the results from affinity determination assays where the sequential binding model were used. Thus, for full-length MCPIP1, we proposed a sequential binding model: oligo + MCPIP1$_{Dimer}$ + MCPIP1$_{dimer}$ ⇌ oligo-MCPIP1$_{dimer}$ + MCPIP1$_{dimer}$ ⇌ oligo-MCPIP1$_{tetramer}$. The presented dissociations constants of the complexes were estimated based on the affinity determination assays shown in Table 2.

for denaturation of proteins, however, the concentration of this osmolyte is sufficient to significantly change the content of bulk water[29]. Urea can substantially influence the polypeptides solvation, increasing protein solvent accessible area which might consequently lead to conformation changes of MCPIP1 and probably its might affect oligomerization[30]. Although, this indirect mechanism appears to be the most likely in our case, there are reports indicating a possible alternative mechanism, in which the urea molecules directly interacts with protein molecules in a divalent manner[31].

The two distinct quaternary structure of MCPIP1 D141N nucleoprotein complexes were also observed in EMSA, using long UTRs fragments as well as single stem loop of the mIL-6$_{82-106}$, as shown by Lipert at al. in Supplementary Fig. 5[21]. Together, the size exclusion chromatography and native PAGE results indicate that the both dimeric and tetrameric forms of MCPIP1 homooligomers were found in the investigated conditions.

Discussion

Previous studies indicated that MCPIP1 is a selective ribonuclease that cleaves translationally active mRNA at the 3′UTR[5]. To determine how MCPIP1 recognizes the unique molecular targets that were reported in biological systems, we applied *in vitro* analysis using recombinant MCPIP1. We identified MCPIP1 as an endoribonuclease that degrades diverse sets of RNA stem-loop structures. Collectively, our data did not indicate a strong structural or sequence preference during *in vitro* cleavage of the RNA stem-loops, as all investigated sequences were affected by MCPIP1. However, our results revealed that unstructured single-stranded RNA is highly prone to cleavage by MCPIP1$_{WT}$. We observed that MCPIP1$_{WT}$-induced degradation of the mIL-6$_{82-106}$ stem-loop starts from the 3′ end of the sequence. Simultaneously, cleavage occurs at the loop site of the stem loop. As a consequence of loop cleavage, the stem-loop structure is destabilized, and ssRNA fragments are generated, which are further processively degraded in the next step (Fig. 6A). Surprisingly, we observed that 6-nt-long ssRNA was not rapidly cleaved by MCPIP1$_{WT}$. A possible explanation for this process might be that the 6 nt RNA substrate is too short to reach the nuclease site. We hypothesized that the region of MCPIP1 that is crucial for RNA binding must be proximal to the catalytic cleft in the PIN domain since the 7-nt-long mIL-6$_{82-88}$ substrate was still bound with high affinity to the PIN$_{D141N}$ domain. We hypothesized that the positively charged region that is present in the structure of the MCPIP1 PIN domain is essential in the RNA recognition

process and protects bound fragments of short ssRNA from further cleavage. Preferential cleavage of oligoribonucle-otides triggered by MCPIP1 was observed for sequences lacking a G nt at positions -1 and $+1$ of the cleavage site, however, this observation might be affected by the low complexity of the analyzed sequences.

Degradation of 3′FAM-labeled oligonucleotides indicated that introduction of the fluorescent label did not disable the recognition of the cleavage sites by $MCPIP1_{WT}$. However, for 3′FAM-labeled oligonucleotides, we observed a decrease in the nucleolytic efficiency of $MCPIP1_{WT}$. Moreover, we observed that MCPIP1 cleaved poly-U ssRNA oligonucleotides in a processive manner. These findings may suggest 3′ to 5′ exonuclease activity of MCPIP1 against ssRNA. Additionally, previous reports revealed that the MCPIP1 PIN domain shares high structural homology with the T5 D15 5′-exonuclease[11,32]. Nevertheless, the successive exonuclease degradation of single-stranded RNA by MCPIP1 is not relevant *in vivo* due to the low rate of observed 3′ to 5′ exonuclease cleavage activity. Moreover, *in vitro* endonuclease activity of recombinant MCPIP1 had a strong background as shown in the results of cleavage of the loop sites of the investigated stem-loops. Additionally, previous results have also shown degradation of longer transcripts, such as IL-6, IL-8 or CEBPβ, which indicated that preferable sites of endonucleolytic cleavage are present in these transcripts[5,6,21]. The endonuclease activity of recombinant MCPIP1 was also confirmed from *in vitro* degradation of circular RNA fragments[5].

We hypothesized that the marginal *in vitro* activity observed here of either $MCPIP1_{WT}$ or $MCPIP1_{D141N}$ towards DNA molecules is irrelevant *in vivo*, since MCPIP1 has a primary cytoplasmic localization and should be considered as a ribonuclease. In contrast, the EndoV nuclease efficiently cleaves both RNA and DNA substrates[33]. There are also evidences of nuclear localization of the MCPIP1 for which essential is nuclear localization signal (RKKP) that is present in amino acid sequence of the MCPIP1[34]. However, observed here DNA cleavage was inefficient thus we estimate DNAse activity of MCPIP1 as biologically insignificant.

Ribonucleases possessing PIN domains usually lack strong sequence specificity in *in vitro* studies with recom-binant proteins[13]. However, protein engineering can modify the specificity of these RNases. One example is the engineered PIN-PUF nuclease that possesses a high sequence specificity of RNA degradation[35]. Most likely, mod-ification of the PIN domain from MCPIP1 will enhance its specificity and will be beneficial for the development of a highly sequence-specific molecular tool.

To the best of our knowledge, the equilibrium dissociation constants of the complex of MCPIP1 with oligo-nucleotides have not been previously described. To investigate oligonucleotides, we determined the K_d values of the complex with $MCPIP1_{D141N}$, $PIN-ZF_{D141N}$ and PIN_{D141N}. The dissociation constant studies revealed a high affinity of $MCPIP1_{D141N}$ to oligonucleotides, however, they did not show a major difference in affinity param-eters using different oligonucleotides. We observed that the affinity of $MCPIP1_{D141N}$ and its fragments towards ssRNA, ssDNA and dsDNA substrates is lower than that for oligonucleotides forming stem loops. Moreover, we did not observe significant differences between the affinity of $MCPIP1_{D141N}$ or $PIN-ZF_{D141N}$ to the investigated oligonucleotides. Therefore, we hypothesized that the PIN-ZF fragment is crucial for maintaining the complex with oligonucleotides. We also observed that the zinc-finger domain significantly increased the affinity of the PIN_{D141N} domain to 25-nt-long oligonucleotides. Interestingly, for shorter oligonucleotides, we did not observe significant differences in the affinity for PIN_{D141N} or $PIN-ZF_{D141N}$. We hypothesized that the zinc finger does not reach short substrates, which were localized in proximity to the catalytic pocket of MCPIP1. A zinc finger teth-ered in the vicinity of the PIN catalytic domain might enhance the re-association of the substrate and facilitate subsequent cleavage. In contrast, previous data suggested that long RNA fragments derived from the C/EBPβ 3′UTR mRNA interact with full-length $MCPIP1_{D141N}$ but not with $PIN-ZF_{D141N}$[21]. We hypothesized that our previ-ous results might be affected by the non-equilibrium conditions of the EMSA method. It is also possible that for maintaining of $PIN-ZF_{D141N}$ interaction with long mRNA fragments, additional domains of MCPIP1 are crucial for the stability of the ternary complex.

Size exclusion chromatography results indicate that MCPIP1 exists in equilibrium between the dimeric and tetrameric state, we proposed a stoichiometric model of the MCPIP1 - RNA interaction. Two molecules of the MCPIP1 dimer interact with a single stem-loop structure (Fig. 6B). Thus, for the full-length MCPIP1, we pro-posed a sequential binding model: $oligo + MCPIP1_{dimer} + MCPIP1_{dimer} \rightleftarrows oligo\text{-}MCPIP1_{dimer} + MCPIP1_{dimer} \rightleftarrows oligo\text{-}MCPIP1_{tetramer}$. We hypothesized that the binding of oligonucleotide substrates induces homooligomeriza-tion of the MCPIP1. Tetrameric oligomerization of the PIN domain was previously shown for Nob1p and PAE2754, where the PIN domains of these proteins form a ring structure with a central hole that is wide enough to accommodate ssRNA or ssDNA but not double-stranded oligonucleotides[36,37]. Nevertheless, further validation of this model of MCPIP1-RNA complex stoichiometry should be performed. Our model is based on size exclu-sion chromatography results and double binding equilibrium observed in the affinity curves. Resolving the qua-ternary structure of MCPIP1 with RNA oligonucleotides is crucial for understanding its detailed mechanism of RNA regulation. To date, there is no resolved holoenzyme structure of any of the PIN domains; thus, further studies of MCPIP1 complexes are highly interesting.

We observed increased rates of degradation of hairpins with short stems, which are consistent with results published by Mino and coworkers from HITS-CLIP analyses where small stem-loops that contained a 3-nt- or 4-nt-long loop motif were predominantly identified in complexes with $MCPIP1_{D141N}$[5]. Recent studies have revealed the importance of UPF1 for cytoplasmic mRNA decay catalyzed by MCPIP1[5]. UPF1 is an RNA hel-icase that participates in degradation of mRNAs with premature termination codons that are crucial for nonsense-mediated mRNA decay (NMD)[38]. SMG6, one of the key proteins for NMD, also contains a PIN domain at the C-terminus that is responsible for ribonucleolytic activity and mRNA turnover[39]. For *in vitro* RNA substrate cleavage induced by recombinant SMG6, the presence of additional proteins with helicase activity is not neces-sary. We showed that MCPIP1 alone is sufficient to unwind and degrade substrates with stem-loop secondary structures *in vitro*. Nevertheless, UPF1 might enhance unwinding of MCPIP1 substrates as an RNA helicase since we observed that degradation of more stable (with low Gibbs free energy) stem-loops was less efficient.

Interaction with UPF1 and other proteins may increase the rate of degradation of selected RNA targets and broaden the recognition potential of the MCPIP1 complex.

Our biochemical studies revealed numerous cleavage sites introduced by recombinant MCPIP1 in the investigated sequences. We found that MCPIP1 induced endonuclease cleavage in the loop motif of stem-loop structures. We hypothesized that the presence of strong and non-sequence-specific interactions with RNA would enable MCPIP1 to efficiently search for the stem-loop elements in transcripts, and identification of a stem-loop would result in endonucleolytic cleavage and transcript destabilization. Nevertheless, MCPIP1 has been identified as selective ribonuclease that cleaves translationally active mRNAs at the 3′UTR. This raises the possibility that additional proteins that are elements of a ternary complex consisting of transcripts and MCPIP1 might determine the final MCPIP1 specificity.

Methods

Cloning and protein purification.
The human *ZC3H12A* gene that encodes MCPIP1 was optimized for efficient expression in *E. coli* strains and ordered as a synthetic gene from GenScript (USA). The cloning, expression and purification of the full-length MCPIP1$_{WT}$ protein and its mutant form MCPIP1$_{D141N}$ were previously described[6]. The procedures for purification of the N-terminus His$_6$-tagged proteins PIN-ZF$_{WT}$ and PIN-ZF$_{D141N}$ (134–327 residues) were described previously[21]. The same methods were used to purify PIN$_{WT}$ and PIN$_{D141N}$ (134–297 residues), which were also tagged with His$_6$ at the N-terminus. Briefly, *E. coli* BL21-CodonPlus-RIL cultures were grown at 37 °C in LB medium until reaching an OD$_{600}$ of 0.5. Protein expression was induced with addition of 0.5 mM IPTG. All proteins were expressed for 3 hours at 37 °C. Full-length MCPIP proteins were purified using ion-exchange chromatography (TMAE) in denaturing conditions. PIN$_{WT}$, PIN$_{D141N}$, PIN-ZF$_{WT}$ and PIN-ZF$_{D141N}$ were purified using Ni-NTA affinity chromatography in denaturing conditions. Finally, all proteins were dialyzed and purified using a gel filtration Superdex 200 prep grade 10/300 (GE Healthcare) column in a buffer comprised of 25 mM Tris, pH 7.9, 300 mM NaCl, 10% (w/v) glycerol, 1 mM DTT, and 0.5 mM EDTA. Chromatography was performed using an Äkta FPLC purification system (Amersham Pharmacia).

Fluorescent-labeled nucleic acid sequences.
The oligonucleotide sequences listed in Table 1 were purchased from Sigma-Aldrich. These oligonucleotides were fluorescently labeled using 6-carboxyfluorescein (6-FAM). The 5′ ends labeling of oligonucleotides were made by attaching 6-FAM to phosphate group of the 5′ terminal nucleotides. The mIL-6$_{82–106}$ 3′FAM labeling was done by coupling 6-FAM to phosphate group of the 3′ terminal nucleotide. Labeled and purified with high-performance liquid chromatography oligonucleotides were purchased from Sigma-Aldrich. The double-stranded mIL-6$_{82–93}$ dsDNA was prepared by mixing mIL-6$_{82–93}$ ssDNA and the complementary oligonucleotide in a 1:1.2 ratio. Subsequently, for dsDNA, oligonucleotides were annealed by heating to 95 °C for 5 minutes and cooled at room temperature. Analysis of RNA secondary structure of the investigated oligonucleotides was performed using the Vienna RNA web server[40].

RNase assays.
In vitro cleavage assays of FAM-labeled oligonucleotides were performed in buffer containing 25 mM Tris-HCl, pH 7.9, 150 mM NaCl, 10% (w/v) glycerol, 2.5 mM MgCl$_2$, 1 mM DTT, 0.5 mM EDTA and 0.05 mM ZnCl$_2$. Labeled oligonucleotides and MCPIP1 protein concentrations were 7.5 µM and 2 µM, respectively. Samples were incubated at 37 °C, and reactions at different time points were stopped by freezing in dry ice. After addition of twofold excess of concentrated loading dye consisting of 95% (w/v) formamide, 0.5 mM EDTA, 0.025% (w/v) xylene cyanol, and 0.025% (w/v) bromophenol blue, reactions products were denatured at 95 °C for 1 minute. An alkaline hydrolysis RNA ladder for each oligonucleotide was generated through denaturation at 95 °C for 25 minutes in alkaline buffer containing 50 mM sodium bicarbonate, pH 9.5, and 1 mM EDTA. Samples were resolved in denaturing gel electrophoresis in TBE (Tris/borate/EDTA) buffer. Denaturing gels contained 20% polyacrylamide and 7.5 M urea. Fluorescence signals were detected using ChemiDoc gel imaging device with ImageLab 5.2 software (BioRad Laboratories). Signal acquisition times 0.5 sec were the same for each of the gels.

Affinity determination assays.
The concentration of FAM-labeled oligonucleotides was 2 nM in a system with MCPIP1$_{D141N}$ and 20 nM in a system containing PIN$_{D141N}$ or PIN-ZF$_{D141N}$ proteins. Free FAM label (6-Carboxyfluorescein, C0662 Sigma-Aldrich) was used as a control of affinity determination assay. Unlabeled and HPLC purified hIL-6$_{81–98}$ RNA oligonucleotide was purchased from Sigma-Aldrich. Protein concentrations were determined by measuring the absorbance at 280 nm using a NanoDrop 2000 spectrophotometer (Thermo Scientific). Proteins absorption coefficients were calculated on the basis of amino acid sequence. Samples were prepared using the twofold serial dilution method; thus, in each sample, the concentration of protein gradually changed. The reaction buffer for detection of sample fluorescence contained 25 mM Tris-HCl pH 7.9, 150 mM NaCl, 5% (w/v) glycerol, 2.5 mM MgCl$_2$, 1 mM DTT, 0.5 mM EDTA and 0.05 mM ZnCl$_2$. Fluorescence signals were collected using the FluoroLog FL3–12 spectrofluorometer (Horiba Jobin Yvon). Excitation and emission wavelengths were 495 nm and 514 nm, respectively. Measurements of fluorescence was performed at 25 °C using a temperature controlled cuvette holder. The dimensions of the quartz cuvette were 3 × 3 mm (Hellma). Dissociation constants (K$_d$) were determined using DynaFit software (version 4.07.111, BioKin)[41]. Determination of the binding model was based on residual distribution of fitted curves and standard deviation of determinated dissociation constants. For calculation of the dissociation constants, a sequential binding model was used: N + P + P $\rightleftarrows$ NP + P $\rightleftarrows$ NPP (N – oligonucleotide, P – protein), where K$_{d1}$ and K$_{d2}$ were equal dissociation constants. Additionally, two binding models were tested. The first one was characterized by K$_{d1}$ ≠ K$_{d2}$, and the second one was simplified to the single equation N + P $\rightleftarrows$ NP. The graph errors represent standard deviations from 3 independent experiments. For statistical analysis of differences between calculated dissociation constants

for oligonucleotide complexes with $MCPIP_{D141N}$, $PINZF_{D141N}$ and PIN_{D141N} one-way ANOVA followed by Tukey's multiple comparison test was used.

Gel filtration assays. Analytical size exclusion chromatography was performed using a Superdex 200 Increase 10/300 GL column (GE Healthcare) that was calibrated with the following protein standards: myoglobin, α-chymotrypsinogen, β-lactoglobulin, ovalbumin, bovine serum albumin, apoferritin and thyroglobulin. The apparent molecular weight of MCPIP1 proteins was determined based on the column calibration curve. For determination of homooligomerization of the analyzed samples, multiple Gaussian peak fits were performed for chromatogram data using OriginPro 2017 software (OriginLab).

Native polyacrylamide gel electrophoresis. Protein samples for native electrophoresis were prepared with the addition of twofold excess of concentrated loading dye that comprised 62.5 mM Tris-HCl, pH 6.8, 25% glycerol, and 1% (w/v) bromophenol blue. The gels contained 300 mM Tris-HCl, pH 8.8, and 6% polyacrylamide (concentrations of acrylamide/bis-acrylamide were 30%/1% w/v). Electrophoresis was performed at 80 V using running buffer containing 25 mM Tris and 192 mM glycine. Gels were stained with Coomassie Brilliant Blue G-250 solution.

Data availability. The datasets analyzed during the current study are available from the corresponding author on reasonable request.

References

1. Mizgalska, D. *et al.* Interleukin-1-inducible MCPIP protein has structural and functional properties of RNase and participates in degradation of IL-1β mRNA. *FEBS J.* **276**, 7386–7399 (2009).
2. Matsushita, K. *et al.* Zc3h12a is an RNase essential for controlling immune responses by regulating mRNA decay. *Nature* **458**, 1185–1190 (2009).
3. Iwasaki, H. *et al.* The IκB kinase complex regulates the stability of cytokine-encoding mRNA induced by TLR–IL-1R by controlling degradation of regnase-1. *Nat. Immunol.* **12**, 1167–1175 (2011).
4. Li, M. *et al.* MCPIP1 down-regulates IL-2 expression through an ARE-independent pathway. *PLoS One* **7**, e49841 (2012).
5. Mino, T. *et al.* Regnase-1 and roquin regulate a common element in inflammatory mRNAs by spatiotemporally distinct mechanisms. *Cell* **161**, 1058–1073 (2015).
6. Dobosz, E. *et al.* MCPIP-1, Alias Regnase-1, controls epithelial inflammation by posttranscriptional regulation of IL-8 production. *J. Innate Immun.* **8,**, 564–578 (2016).
7. Monin, L. *et al.* MCPIP1/Regnase-1 restricts IL-17A- and IL-17C-dependent skin inflammation. *J. Immunol.* **198**, 767–775 (2017).
8. Lipert, B. Monocyte chemoattractant protein-induced protein 1 impairs adipogenesis in 3T3-L1cells. *Biochim. Biophys. Acta - Mol. Cell Res.* **1843**, 780–788 (2014).
9. Lu, W. *et al.* MCPIP1 selectively destabilizes transcripts associated with an antiapoptotic gene expression program in breast cancer cells that can elicit complete tumor regression. *Cancer Res.* **76**, 1429–40 (2016).
10. Marona, P. *et al.* MCPIP1 downregulation in clear cell renal cell carcinoma promotes vascularization and metastatic progression. *Cancer Res.* **77**, 4905–4920 (2017).
11. Xu, J. *et al.* Structural study of MCPIP1 N-terminal conserved domain reveals a PIN-like RNase. *Nucleic Acids Res.* **40**, 6957–6965 (2012).
12. Senissar, M., Manav, M. C. & Brodersen, D. E. Structural conservation of the PIN domain active site across all domains of life. *Protein Sci.* **26**, 1474–1492 (2017).
13. Matelska, D., Steczkiewicz, K. & Ginalski, K. Comprehensive classification of the PIN domain-like superfamily. *Nucleic Acids Res.* **45**, 6995–7020 (2017).
14. Lebreton, A., Tomecki, R., Dziembowski, A. & Seraphin, B. Endonucleolytic RNA cleavage by a eukaryotic exosome. *Nature* **456**, 993–996 (2008).
15. Winther, K. S., Brodersen, D. E., Brown, A. K. & Gerdes, K. VapC20 of Mycobacterium tuberculosis cleaves the sarcin-ricin loop of 23S rRNA. *Nat. Commun.* **4**, 2796 (2013).
16. Habacher, C. *et al.* Ribonuclease-mediated control of body fat. *Dev. Cell* **39**, 359–369 (2016).
17. Liang, J. *et al.* A novel CCCH-zinc finger protein family regulates proinflammatory activation of macrophages. *J. Biol. Chem.* **283**, 6337–6346 (2008).
18. Fu, M. & Blackshear, P. J. RNA-binding proteins in immune regulation: a focus on CCCH zinc finger proteins. *Nat. Rev. Immunol.* **17**, 130–143 (2017).
19. Yokogawa, M. *et al.* Structural basis for the regulation of enzymatic activity of Regnase-1 by domain-domain interactions. *Sci. Rep.* **6**, 22324 (2016).
20. Suzuki, H. I. *et al.* MCPIP1 ribonuclease antagonizes dicer and terminates microRNA biogenesis through precursor microRNA degradation. *Mol. Cell* **44**, 424–436 (2011).
21. Lipert, B., Wilamowski, M., Gorecki, A. & Jura, J. MCPIP1, alias Regnase-1 binds and cleaves mRNA of C/EBPβ. *PLoS One* **12**, e0174381 (2017).
22. Jeltsch, K. M. *et al.* Cleavage of roquin and regnase-1 by the paracaspase MALT1 releases their cooperatively repressed targets to promote TH17 differentiation. *Nat. Immunol.* **15**, 1079–1089 (2014).
23. Leppek, K. *et al.* Roquin promotes constitutive mRNA decay via a conserved class of stem-loop recognition motifs. *Cell* **153**, 869–81 (2013).
24. Sgromo, A. *et al.* A CAF40-binding motif facilitates recruitment of the CCR4-NOT complex to mRNAs targeted by Drosophila Roquin. *Nat. Commun.* **8**, 14307 (2017).
25. Masuda, K. *et al.* Arid5a regulates naive $CD4^+$ T cell fate through selective stabilization of Stat3 mRNA. *J. Exp. Med.* **213**, 605–619 (2016).
26. Zuker, M. Mfold web server for nucleic acid folding and hybridization prediction. *Nucleic Acids Res.* **31**, 3406–3415 (2003).
27. Crooks, G. E., Hon, G., Chandonia, J.-M. & Brenner, S. E. WebLogo: a sequence logo generator. *Genome Res.* **14**, 1188–1190 (2004).
28. Arcus, V. L., McKenzie, J. L., Robson, J. & Cook, G. M. The PIN-domain ribonucleases and the prokaryotic VapBC toxin-antitoxin array. *Protein Eng. Des. Sel.* **24**, 33–40 (2011).
29. Salvi, G., De Los Rios, P. & Vendruscolo, M. Effective interactions between chaotropic agents and proteins. *Proteins Struct. Funct. Bioinforma.* **61**, 492–499 (2005).
30. Bhuyan, A. K. Protein stabilization by urea and guanidine hydrochloride. *Biochemistry* **41**, 13386–94 (2002).
31. Zhang, Y. & Cremer, P. S. Chemistry of Hofmeister Anions and Osmolytes. *Annu. Rev. Phys. Chem.* **61**, 63–83 (2010).
32. Ceska, T. A., Sayers, J. R., Stier, G. & Suck, D. A helical arch allowing single-stranded DNA to thread through T5 5′-exonuclease. *Nature* **382**, 90–93 (1996).

33. Vik, E. S. *et al.* Endonuclease V cleaves at inosines in RNA. *Nat. Commun.* **4**, 2271 (2013).
34. Zhou, L. *et al.* Monocyte chemoattractant protein-1 induces a novel transcription factor that causes cardiac myocyte apoptosis and ventricular dysfunction. *Circ. Res.* **98**, 1177–85 (2006).
35. Wang, Y., Wang, Z. & Tanaka Hall, T. M. Engineered proteins with Pumilio/fem-3 mRNA binding factor scaffold to manipulate RNA metabolism. *FEBS J.* **280**, 3755–67 (2013).
36. Arcus, V. L., Bäckbro, K., Roos, A., Daniel, E. L. & Baker, E. N. Distant structural homology leads to the functional characterization of an archaeal PIN domain as an exonuclease. *J. Biol. Chem.* **279**, 16471–8 (2004).
37. Fatica, A., Tollervey, D. & Dlakić, M. PIN domain of Nob1p is required for D-site cleavage in 20S pre-rRNA. *RNA* **10**, 1698–701 (2004).
38. Conti, E. & Izaurralde, E. Nonsense-mediated mRNA decay: molecular insights and mechanistic variations across species. *Curr. Opin. Cell Biol.* **17**, 316–325 (2005).
39. Glavan, F., Behm-Ansmant, I., Izaurralde, E. & Conti, E. Structures of the PIN domains of SMG6 and SMG5 reveal a nuclease within the mRNA surveillance complex. *EMBO J.* **25**, 5117–25 (2006).
40. Hofacker, I. L. Vienna RNA secondary structure server. *Nucleic Acids Res.* **31**, 3429–31 (2003).
41. Kuzmič, P. Program DYNAFIT for the analysis of enzyme kinetic data: application to HIV proteinase. *Anal. Biochem.* **237**, 260–273 (1996).

Acknowledgements

Author Contributions

M.W., A.G. and J.J. designed the research. M.W. performed the experiments. M.W., A.G. and J.J. analyzed the data. M.W. and J.J. wrote the paper. M.W., A.G., M.D.W. and J.J. commented on the manuscript.

Additional Information

Supplementary information accompanies this paper at https://doi.org/10.1038/s41598-018-25765-2.

Competing Interests: The authors declare no competing interests.

Publisher's note: Springer Nature remains neutral with regard to jurisdictional claims in published maps and institutional affiliations.